Composite Structures 254 (2020) 112855

Contents lists available at ScienceDirect

Composite Structures

journal homepage: www.elsevier.com/locate/compstruct

Twist morphing of a composite rotor blade using a novel metamaterial

Huaiyuan Gu [a,*], Alexander D. Shaw [a], Mohammadreza Amoozgar [b], Jiaying Zhang [a], Chen Wang [a], Michael I. Friswell [a]

[a] College of Engineering, Swansea University, Swansea SA2 8PP, United Kingdom
[b] School of Computing and Engineering, University of Huddersfield, HD1 3DH, United Kingdom

ARTICLE INFO

Keywords:
Metamaterial
Composite rotor blade
Twist morphing
Bend-twist coupling
FE analysis

ABSTRACT

A novel meta-material has been designed and implemented into a rotor blade to enhance aerodynamic efficiency by achieving a passive twist during rotation. The twist is induced by bend-twist coupling exhibited in the meta-material, which is created to possess anisotropic elastic properties at the bulk level. A concept design of a rectangular blade spar is proposed where the metamaterial is used as the core material to induce twist. Using finite element analysis(FEA) we demonstrate how the bend-twist property of the blade spar is governed by cell geometries of the core material. The twist is activated by a lagwise bending moment generated from a movable mass at the blade tip due to off-centre centrifugal forces. The relationship between the twist, mass location and rotational speed has been explored. Moreover, it was found that the bend-twist property achieved by the proposed blade spar is more effective compared to that of an anisotropic thin-walled composite beam.

1. Introduction

Morphing blades have drawn increasing attention in past decades, due to their promising aerodynamic performances such as a high aerodynamic efficiency and reduced vibration [1,2]. Blades are able to change their shapes such as twist, camber and pitch, in order to fly optimally in different flight conditions [3–5]. A new concept of introducing morphing in a helicopter blade, inertial twist, has been proposed recently [6], where blade twist was induced by the bend-twist coupling of composite laminate and actuated using a movable mass at the tip of the blade. However, the twist obtained using this concept was highly constrained by the limited bend-twist coupling that can be achieved in the composite material. Thus, there is a need to create an innovative material that is capable of inducing the coupling more efficiently.

A wide range of technologies have been developed to achieve shape morphing with reduced penalties in terms of the complexity and weight such as implementing multistable structures, smart materials or anisotropic skins [7–10]. As an example smart material, piezoelectric materials are able to deform under an electric field and have often been attached to the surfaces of composite structures to induce a strain field. Chen and Chopra [11] twisted a rotor blade by embedding arrays of angled piezoelectric actuators on two opposite sides of the blade surfaces, where approximately 0.5 degree of tip twist was seen in their experiment. The potential of shape memory alloys such as nickel titanium alloy, has also been explored, where the shape can be manipulated by temperature due to the phase transformation [12]. Ameduri and Concilio [13] discussed the implementation of a shape memory alloy tube, which was able to generate a torque during the strain recovery process, and thereby induce a blade twist.

Self-adaptive morphing achieved by elastic coupling of composite materials have attracted considerable interest [14]. Chandra et al. [15] experimentally characterised the twist produced by a thin-walled composite beam wrapped with symmetric and antisymmetric layup configurations, where bend-twist and extension-twist coupling were achieved respectively. The work demonstrated the relationship between structural coupling and layup configurations, suggesting that a desired twist could be obtained by tailoring the composite plies with a specific layup configuration. The aeroelastic instability of these elastic coupled beams was reported in the work of Don et al. [16], where the limits on the amount of coupling required to maintain a positive definiteness were established. The Grumman X-29 was a forward-swept wing aircraft, that used stiffness tailored composite laminates to eliminate aeroelastic divergence via bend-twist coupling [17].

Cellular materials allow superior mechanical properties to be reached at a very low density such as high stiffness, damage tolerance and energy absorption [18–21]. Several concepts have been developed to explore their potential in morphing aircraft. For example, a chiral

* Corresponding author.
E-mail address: huaiyuan.gu@swansea.ac.uk (H. Gu).

https://doi.org/10.1016/j.compstruct.2020.112855
Received 3 May 2020; Revised 16 July 2020; Accepted 13 August 2020
Available online 26 August 2020

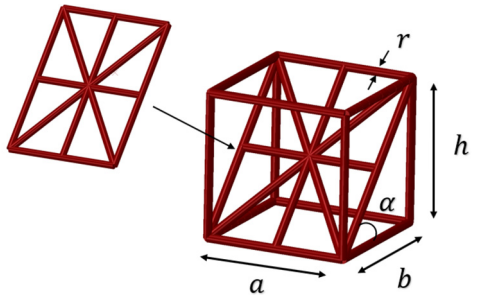

Fig. 1. Unit cell of the three-dimensional bend-twist metamaterial.

structure was implemented into an airfoil by Bettini et al. [22], which allowed a large overall displacement to be produced with a small strain in the struts. They demonstrated that a large downward displacement of the trailing edge could be obtained at a relatively low air speed due to the superior deformability of the structure [23]. A similar concept was also proposed in the work of Heo et al. [24], where honeycomb airfoils were created with various topologies including regular, auxetic and chiral meso-structures, to allow effective passive morphings under fluid-structural interactions. Compression-torsion coupling was exhibited by a recently developed three-dimensional metamaterial [25], where its unit cell included inclined rods allowing torsion to be induced from axial compression. The compression-torsion property can also be obtained from other topologies based on similar deformation mechanisms such as Kirigami cellular structures and tetrachiral cylindrical tubes [26,27]. Zheng et al. [28] proposed a metamaterial which exhibited a significant tension–torsion coupling. The material was created by stacking layers tetra-chiral honeycomb using a series of inclined rods. Approximately 10° twist angle was measured from a uniaxial tensile test with an applied axial strain of 1%. A unique tension-shear coupling was seen in the tetrachiral lattice where the structure undergoes shear deformation with respect to a tensile loading [29].

Wu and co-workers [30] reviewed a large body of metamaterials and discussed their potential in multifunctional applications. Despite a wide range of unique mechanical properties achieved by the existing materials, few topologies offer bend-twist coupling. Hence the present work aims to create such a material which possesses an effective bend-twist property, and thereby can be used as a deployable candidate for the inertial twist morphing concept. The proposed unit cell is shown in Fig. 1, which is composed of a simple cube and a triangulated sub-cell along the diagonal with inclination angle, α. The purpose of the diagonal sub-cell is to modify the symmetric planes of the cube which lead to anisotropic elastic properties. The topology of the sub-cell is constructed from combined squares and triangles leading to a quasi-isotropic modulus [31] which provides an increased rigidity in the transverse direction of the cell. Based on the unit cell configuration, the relative density, $\bar{\rho}$, can be calculated as:

$$\bar{\rho} = \frac{2a + b + h + 2\sqrt{b^2 + h^2} + 2\sqrt{a^2 + b^2 + h^2}}{abh}\pi r^2 \tag{1}$$

This paper is arranged as follows. The elastic properties of the metamaterial is characterised in Section 2. Section 3 presents a concept design of a rectangular blade spar, where a comparison was also

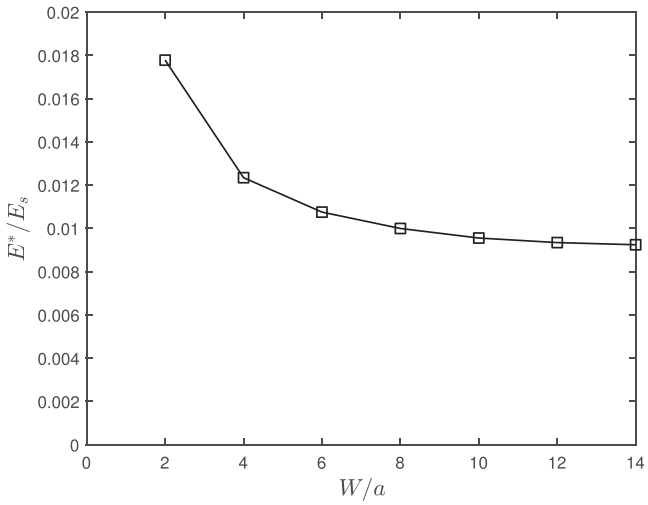

Fig. 3. Normalised modulus of the metamaterial created with different numbers of cells.

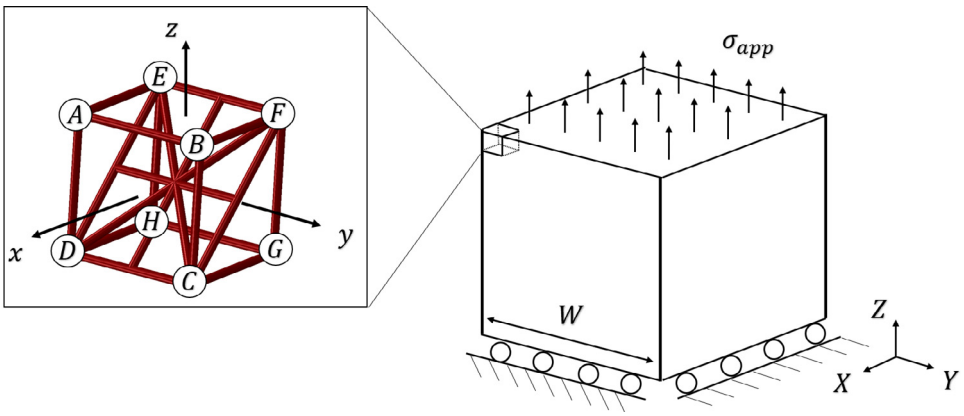

Fig. 2. Unit cell of the stiffness tailored rectangle.

Table 1
Cell dimensions and material properties [33] used in the model.

r	a	E_s	ν	σ_y
0.25 mm	5 mm	70000 MPa	0.33	255 MPa

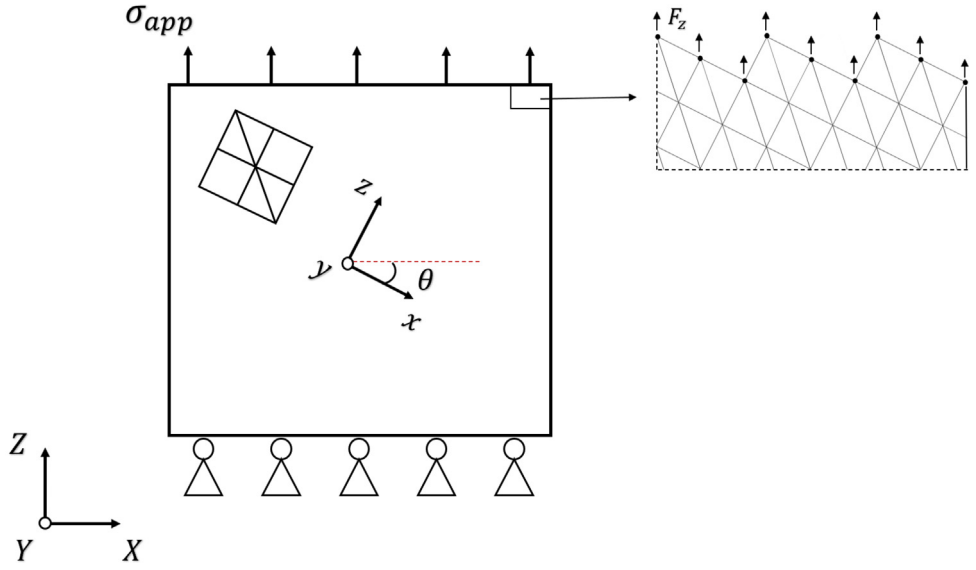

Fig. 4. FE model of the metamaterial created with different cell orientations.

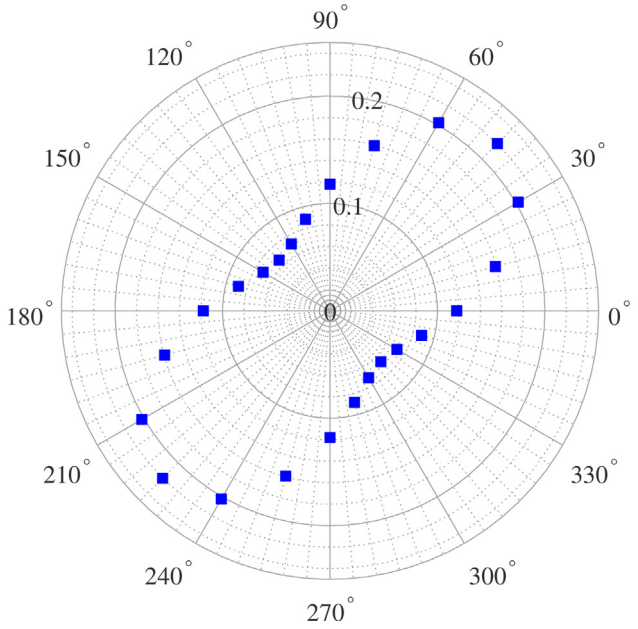

Fig. 5. Polar plot of the normalised Young's modulus, $E^*/E_s\bar{\rho}$.

presented between the bend-twist property obtained from the new design and a thin-walled composite beam. Section 4 reveals the limits on the twist that can be achieved for the blade spar. The final section explains a mechanism which is adopted to activate twist during blade rotation.

2. Elastic modulus

A numerical analysis was conducted using the commercial FE package ABAQUS 2017 [32] to investigate the elastic modulus of the material. A number of cubic models were created where the normalised width, W/a, was ranged from 2 to 14, as shown in Fig. 2. The X, Y, Z axes represent the coordinates of the global geometry, while the x, y, z axes represent the local coordinates of the unit cell. The unit cell was created in a cubic shape where $a = b = h$. Each strut was made with a circular cross section and modelled using 10 Timoshenko beam elements (element code B31 in ABAQUS) to ensure mesh independence. The constituent material was assumed to be aluminium 6082 whose properties, including modulus, E_s, Poisson's ratio, ν, and yield strength, σ_y, are listed in Table 1. A uniform stress was applied on the top face while only the vertical motion of the bottom face was constrained. The modulus was calculated by dividing the uniaxial strain from the applied stress, σ_{app}. The numerical results are presented in Fig. 3, where the elastic modulus of the metamaterial, E^*, is normalised by the modulus of the constituent material, E_s. It was noted that E^* reduces asymptotically with an increase in W/a, and approaches to a size-independent value when $W/a > 12$.

To investigate the anisotropy of the elastic modulus, analysis was performed using the model created with different cell orientations defined by angle θ, as shown in Fig. 4, while the global dimensions of the model remained identical. The model width, W/a, was chosen to be 25 to minimise the influence of the boundary layer illustrated in the Fig. 4 and ensure that size independent properties can be obtained for each orientation. The obtained results are presented using a polar plot, shown in Fig. 5. It was found that the elastic modulus increases with cell orientation, θ, and reached the maximum value at 45° as shown in Fig. 5. This is caused by the change of load distribution within the unit cell. The applied stress, σ_{app}, was predominantly carried by the simple cube among the struts 'A–D', 'B–C', 'F–G' and 'E–H' when the angle θ was small. When the cell orientation approaches 45°, the load was gradually shifted from the cube to the triangulated sub cell which possesses a higher stiffness compared to the simple cube due to its higher number of load paths. Applying a uniaxial tensile load along the x-axis, a coupled shear strain, ε_{xz}, was induced as shown in Fig. 6. Consequently, twist can be achieved when a bending moment about the z-axis is applied to the material as a result of the opposite signs of the shear strain, ε_{xz}, occurring in the tensile and compressive regions.

3. Bend-twist coupled spar

A concept design of a rectangular blade spar is presented in Fig. 7, where the dimensions of the cross-section i.e. width, W, and thickness, t, are determined based on a Bo105 main rotor blade [34] and the length, L, is chosen to be 500 mm. The spar was designed into a sandwich structure which used the bend-twist coupled metamaterial as the core material. The skin was made of two layers of 0° Hexcel 8522 IM7 carbon fibre laminate, to enhance the bending stiffness and carry the

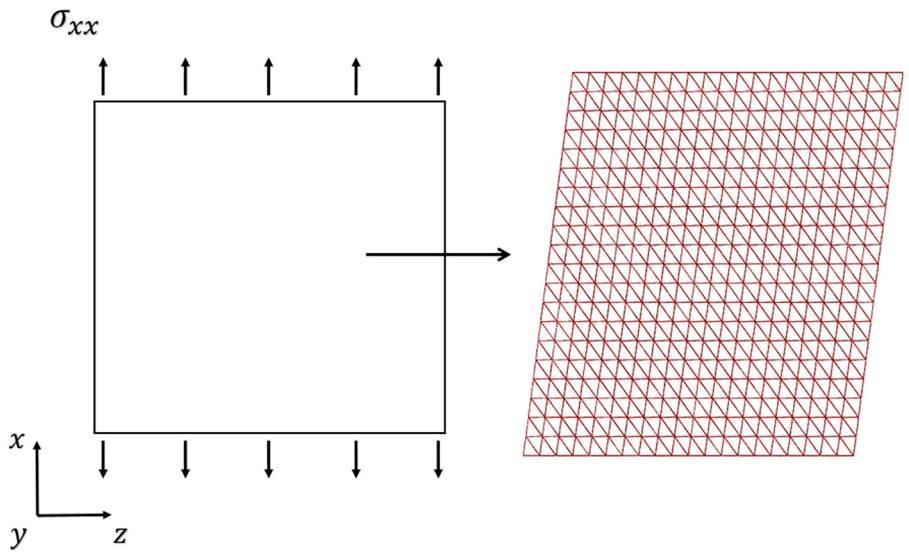

Fig. 6. Deformed metamaterial under uniaxial tensile load.

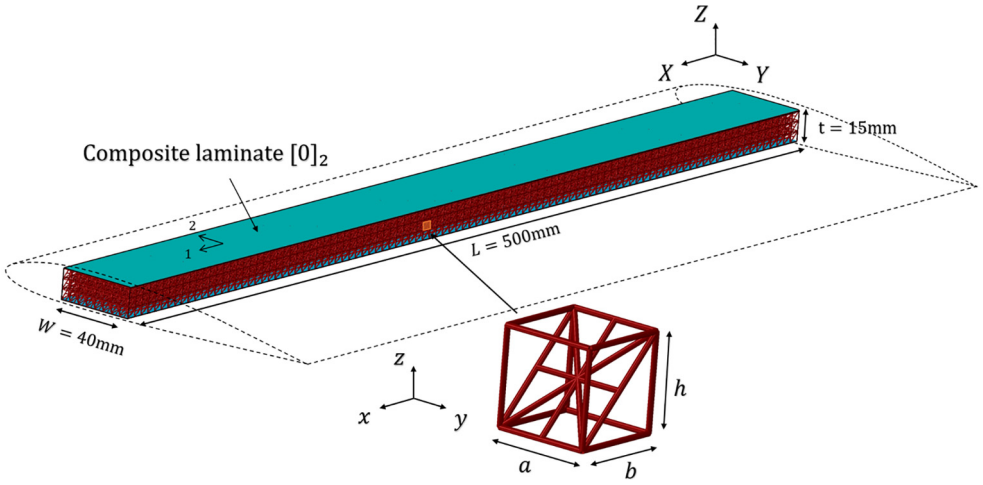

Fig. 7. Schematic drawing of the morphing spar composed of composite laminates (skin) and metamaterial (core).

Table 2
Layup configuration and material properties of the composite skin.

Layup	E_{11}	E_{22}	G_{12}	ν_{12}	t	ρ
$[0]_2$	154 GPa	8.96 GPa	5.316 GPa	0.32	0.125 mm	1.6 g/cm^3

axial centrifugal forces caused by rotation. The mechanical properties, ply thickness, t, and density, ρ, of the laminate are shown in Table 2.

Numerical analysis has been conducted to determine the bend-twist property achieved by the blade spar. The cell configurations and material properties used in this analysis were identical to those in Section 2, as shown in Table 1. The composite laminates were modelled using conventional shell elements (element code S4R in ABAQUS). The core material and composite skins were assembled in the model using tie constraint to avoid computational error caused by the transition of the two different element types [32]. More specifically, the top and bottom surfaces of the metamaterial were constrained to have equal displacements at the laminate surfaces to replicate an ideal bonding condition. Fig. 8 shows the deformed configuration of the blade spar when a lagwise bending moment of 1Nm is applied at the tip. The contour indicates the out of plane displacement field, U_z, from which the spanwise distribution of twist was calculated i.e. dividing the differences in U_z between two opposite spanwise edges by the spar width, W. It was noted that the boundaries of the section remained straight before and after the deformation, and the composite laminates at the top and bottom surfaces were subjected to a combined bending and torsion due to the coupling effect exhibited in the core material.

Furthermore, the analysis was extended to examine the bend-twist coupling of the blade spar created with modified cell configurations i.e. the aspect ratio of the unit cell was changed by increasing cell length, b. Figs. 9 and 10 illustrate the distributions of the deflection and twist of the blade spar created with different core materials. Upon a lagwise bending moment, the twist increased linearly from the hub to tip. It is noted that the twist induced by a given bending moment increases with the aspect ratio of the core material, while their deflection curves were identical. This is attributed to the change of lagwise bending, $\overline{EI}$, and torsional rigidity, $\overline{GJ}$, in response to the change of the aspect ratio.

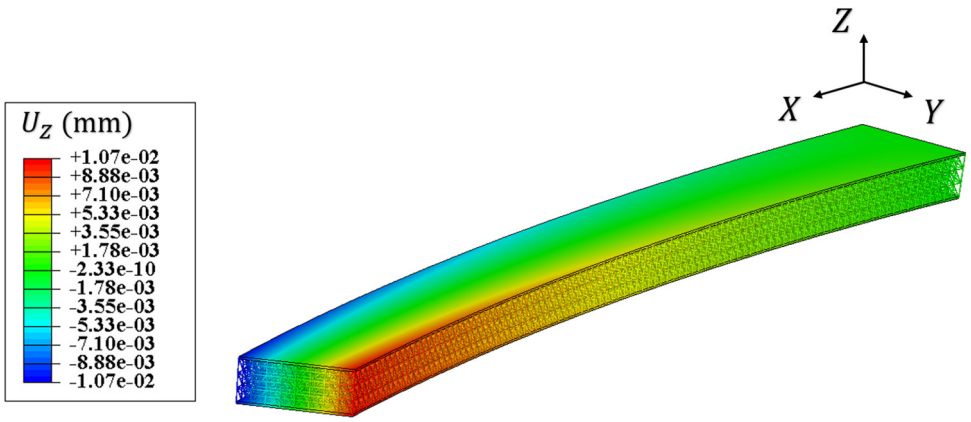

Fig. 8. The out of plane displacement field of the spar (Case 1) subjected to a lagwise bending moment of 1 Nm.

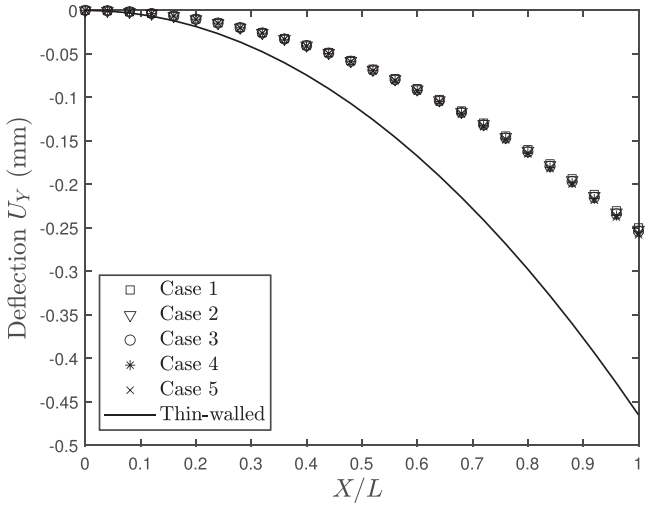

Fig. 9. Distribution of bending deflection of the spar created with different core materials subjected to a lagwise bending moment of 1 Nm.

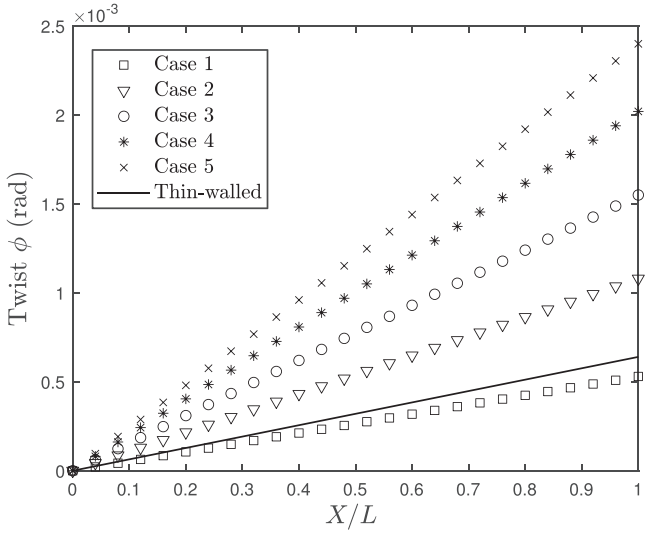

Fig. 10. Distribution of twist of the spar created with different core materials subjected to a lagwise bending moment of 1 Nm.

The bending and torsional rigidity can be calculated based on the physical reasoning that forces and moments induced in the beam cross section were evaluated under a unitary deformation [35]. It was found that the increase in the aspect ratio, b/a, led to a reduced torsional rigidity, $\overline{GJ}$, as illustrated in Table 3. This is attributed to the reduction of the inclination angle, α, between the sub-cell and beam axis as shown in Fig. 7. The model also revealed that the bending moment was predominantly carried by the axial stresses in the struts 'A–E', 'B–F', 'C–G' and 'D–H', and hence the bending rigidity, $\overline{EI}$, was determined by the number of cells contained in the cross-section ($Y-Z$ plane) which was not affected by the change of cell length, b.

Next, the influence of the strut radius, r, upon the twist was investigated. A thick strut radius will not only cause an increased overall weight, but also a higher bending and torsional stiffness, thereby a greater bending moment can be required to induce a targeted twist. However, a material created with an extremely low strut radius, r, can fail to overcome the torsional stiffness of the beam cross-section. Therefore a numerical parametric study was performed to obtain an optimum strut radius, r, where the maximum twist can be reached at a given bending moment.

Three types of beam configurations were used in this analysis corresponding to Cases 3, 4 and 5 shown in Table 3, while the strut radius, r, was varied from 0.05 mm to 0.3 mm. The tip deflection and twist were evaluated when a lagwise bending moment of 1 Nm was applied at the tip, as shown in Figs. 11 and 12. The deflection at the tip reduces linearly with r^2 which was attributed to the increased bending stiffness of the core material. While the tip twist was low when the strut radius was 0.05 mm indicating the core material was over compliant to induce sufficient torque. However, the twist increased significantly for $r = 0.1$ mm and reached the maximum value at $r = 0.15$ mm. A further increase in the strut radius, r, resulted in a reduction in the twist suggesting $r = 0.15$ mm is the optimum strut radius for this beam configuration.

The bend-twist property achieved in the designed blade spar was compared to that exhibited in a thin-walled composite beam model, which is often used during the construction of helicopter blade. A thin-walled beam model was created with the same dimensions as the rectangular spar shown in Fig. 7. The beam was wrapped using a symmetric layup configuration using 45° plies [15], where the plies on the two opposite faces were mirror images with respect to the symmetric plane of the geometry shown in Fig. 13.

A bending moment of 1 Nm was applied at the tip of the thin-walled beam model while the other end was fixed in all directions. The distribution of the spanwise deflection and twist are presented in Figs. 9 and 10. It is noted that the bending deflection of the thin-walled beam was almost double that of the rectangular spar, while the bending induced twist was only close to that of the Case 1 configuration.

Table 3
Effective lagwise bending and torsional rigidity of the spar created with different cell lengths.

Configuration	a (mm)	b (mm)	r (mm)	$\overline{GJ}$ (N m^2)	$\overline{EI}$ (N m^2)	Mass (g)
Case 1	5	5	0.25	20.1	513	80
Case 2	5	10	0.25	18.3	513	61
Case 3	5	15	0.25	15.9	513	56
Case 4	5	20	0.25	12.8	513	53
Case 5	5	25	0.25	10.7	513	52

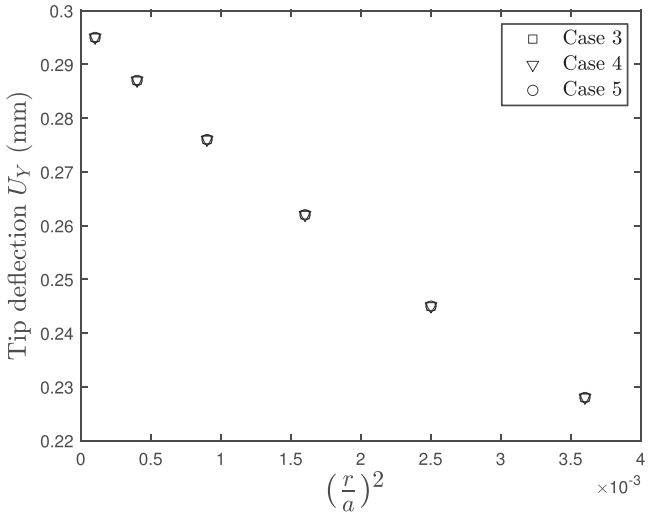

Fig. 11. Tip deflection of the beam created with different strut radius in the core material.

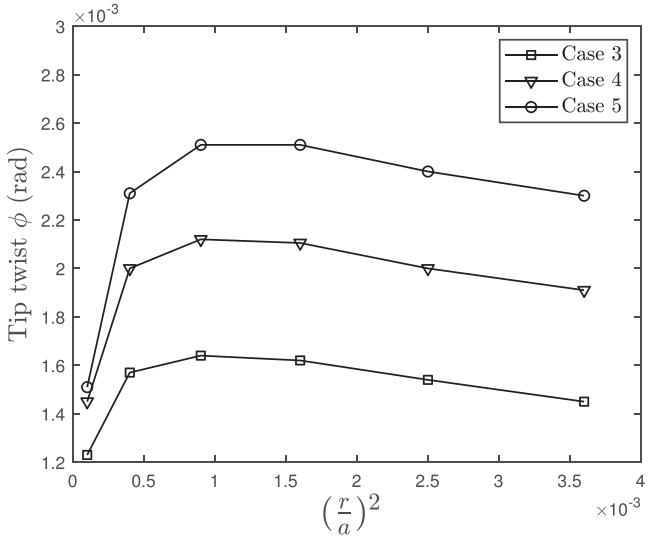

Fig. 12. Tip twist of the beam created with different strut radius in the core material.

Furthermore, the overall mass of the thin-walled beam is equal to 66 g which is close to the mass of the Case 2 configuration. Approximately 20% lower masses were found in the configurations of Cases 3, 4 and 5, as shown in Table 3. The results suggest that a more effective bend-twist property is achieved in the proposed beam configuration compared to the thin-walled composite beam, and the metamaterial presented in this study can be utilized as a lighter solution to produce elastic coupling.

4. Failure analysis

This section aims to investigate the failure mode of the beam subjected to a tip bending load and evaluate the limit of twist that can be achieved in different core material configurations. The flexural strength of the spar is highly constrained by the failure strength of the core material. When a bending moment is applied to the beam, the applied load is predominantly balanced by tensile and compressive axial stresses within the struts along the spanwise direction. A core material created with a high density metamaterial tends to fail by plastic yielding of the struts under a tensile load, while in the case of a low density material, buckling can occur prior to the yield failure at the compressive side of the beam. Therefore the failure mode of the beam is dictated by the magnitude of the yield strength, σ_y, and critical buckling stress, σ_b.

Upon a lagwise bending moment, the most heavily loaded struts were seen at the side surfaces of the beam shown in Fig. 14, where the red and blue colors indicate tensile and compressive forces respectively. The tensile failure occurs when the maximum axial stress reaches the yield strength of the consitituent material, σ_y. While the critical buckling stress, σ_b, can be evaluated based on Euler's critical load,

$$\sigma_b = \frac{\pi E_s I_s}{(K_e b r)^2} \tag{2}$$

where E_s and I_s represent the modulus of the constituent material and the second moment of area of the strut. The effective length factor, K_e, was chosen to be 0.65 where both ends of the strut were assumed to be clamped, due to the limited rotation of the nodes in the model. As shown in Fig. 15, the critical axial stress, σ_c, is related to the slenderness ratio, b/r, of the strut. The critical axial stress, σ_c, is switched from strength-controlled to buckling controlled when the slenderness ratio increases, where the transition value can be expressed as:

$$\left(\frac{b}{r}\right)_T = \frac{\pi}{2}\sqrt{\frac{E_s}{\sigma_y K_e}} \tag{3}$$

In the buckling-controlled region, the critical stress, σ_c, reduces dramatically with b/r indicating the flexural strength is also decreased. FE analysis was performed to evaluate the critical bending moment of the spar based on the calculated critical axial stress, σ_c, given in Fig. 15, where the corresponding twist angle was obtained. Fig. 16 presents the tip twist under the critical bending moment for the spars created with different core material configurations. It shows that the limit of twist increases with strut radius, r, as the struts are capable of withstanding a higher axial load. The failure mode for $r = 0.15$ mm is predominantly buckling-controlled, and therefore the maximum twist that can be achieved reduces with increasing cell length, b. While for $r > 0.15$, the failure mode is strength-controlled at low aspect ratio, b/a, which is then switched to buckling-controlled when the aspect ratio, b/a, increases. Consequently the limit twist increases with b/a at the beginning of the curve, but reduces as soon as the buckling occurs. Therefore the transition slenderness ratio, $\left(\frac{b}{r}\right)_T$, can be considered as an optimum design, when a large twist angle is essential.

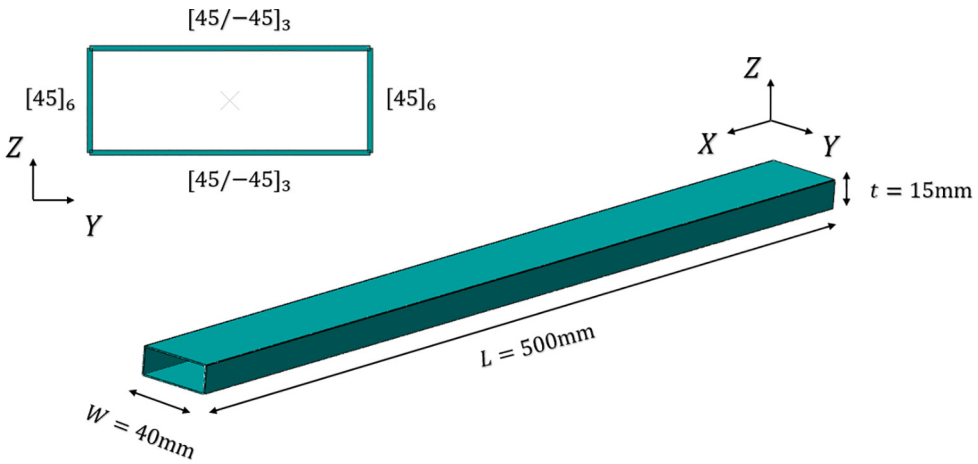

Fig. 13. Thin-walled composite beam model created with 45° symmetric layup.

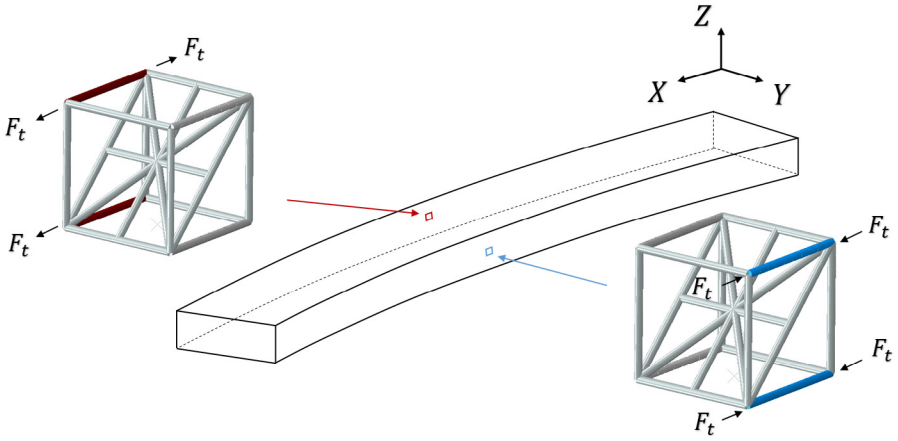

Fig. 14. Loading condition on the most heavily loaded strut under bending.

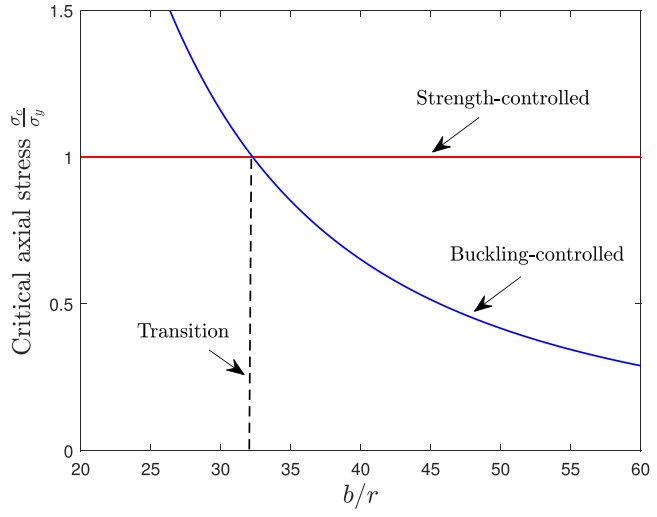

Fig. 15. Critical axial load for different strut slenderness.

5. Twist actuation

This section examines a mechanism which is used to induce bending moment during rotation, and thereby activate the twist. This is achieved by adding a movable mass at the tip of the wing box [6] which causes lagwise bending produced by centrifugal forces as shown in Figs. 17 and 18. The magnitude of the bending moment is adjusted by manipulating the distance between the mass and the shear centre of the cross section. The magnitude of the centrifugal force, F_c, can be related to the mass, m_p, and the chordwise location, y_p,

$$F_c = m_p \omega^2 \sqrt{\left(y_p^2 + L^2\right)} \tag{4}$$

where ω represents the rotational speed. The corresponding bending moment can be calculated as,

$$M_z = F_c \cos\beta y_p - F_c \sin\beta (L - X) \tag{5}$$

Substituting $\cos\beta$ and $\sin\beta$ into Eq. (5) and using y_p and L yields,

$$M_z = \frac{F_c y_p X}{\sqrt{L^2 + y_p^2}} \tag{6}$$

Eq. (6) shows that the bending moment induced by the concentrated mass increases linearly with the spanwise distance, X. Therefore the corresponding twist rate, $\frac{d\phi}{dX}$, can be expressed as,

$$\frac{d\phi}{dX} = \frac{A_0 F_c y_p X}{\sqrt{L^2 + y_p^2}} \tag{7}$$

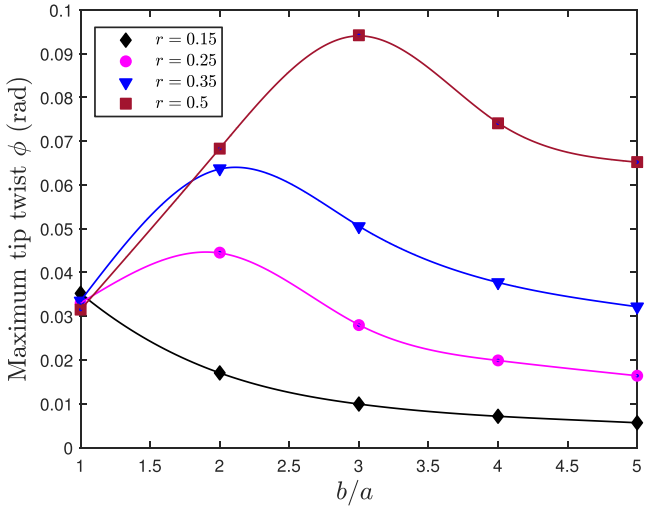

Fig. 16. Twist limit for the spar created with different core materials.

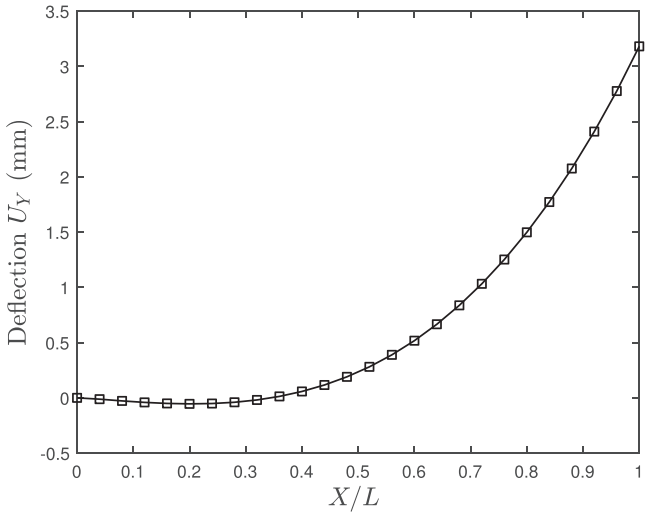

Fig. 19. The deflection profile of the blade spar for the Case 5 configuration ($\omega = 1000$ rpm, $m_p = 100$ g, $y_p = 80$ mm).

where the coefficient A_0 depends on the configuration of the core material. Integrating both sides Eq. (7), the distribution of the spanwise twist may be written as,

$$\phi = \frac{A_0 F_c y_p X^2}{2\sqrt{L^2 + y_p^2}} \tag{8}$$

For $L \gg y_p$, Eq. (8) can be further simplified as,

$$\phi = \frac{A_0 F_c y_p X^2}{2L} \tag{9}$$

The above indicates that the twist distribution induced by a tip movable mass increases quadratically from the hub to tip and changes linearly with the mass location, y_p, and centrifugal force, F_c.

To validate the analytical prediction, a numerical analysis has been conducted to characterise the deformation of the spar for the mass, m_p, and chordwise location, y_p. The configuration of the core material was based on Case 5 given in Table 3, and the material properties were identical to those in Section 2 as shown in Table 1.

An inertial mass of 100 g was added at the tip with $y_p = 80$ mm and a rotational body force was applied to the whole beam with specified angular velocity of 1000 rpm. Figs. 19 and 20 present the predicted spanwise deflection and twist. It is noted that the rate of twist increases quadratically with the spanwise distance, X, as suggested by the analytical prediction given in Eq. (9). It was found that applying the rotational body force at the tip without considering the influence of the mass of the beam itself gave the same result. This indicates that the centrifugal force generated by the beam mass is symmetric about the rotational axis and therefore has no contribution to the lag bending and twist.

The analysis was then extended to evaluate the tip twist of the blade spar attached with different masses, m_p, with changing chordwise locations, y_p. Fig. 21 shows that the tip twist increases with the mass, m_p, and changes linearly with the mass location, y_p. Furthermore, it is noted that a considerable twist was obtained by using a reasonably small mass, m_p.

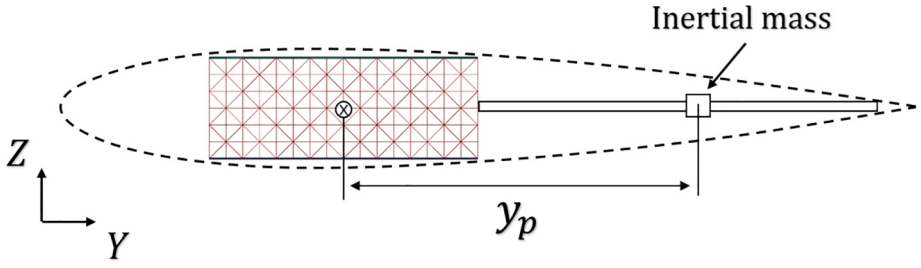

Fig. 17. Cross-section of the blade with an inertial mass moving along chord wise direction.

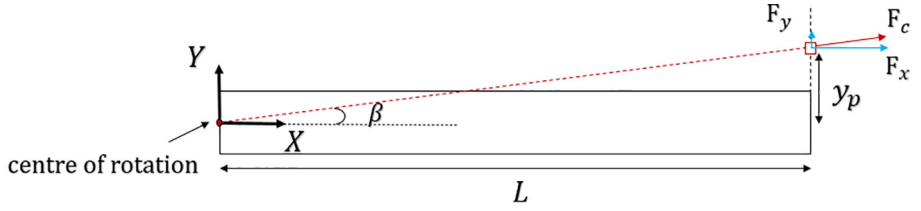

Fig. 18. Angle between the centrifugal force and spanwise direction of the blade spar.

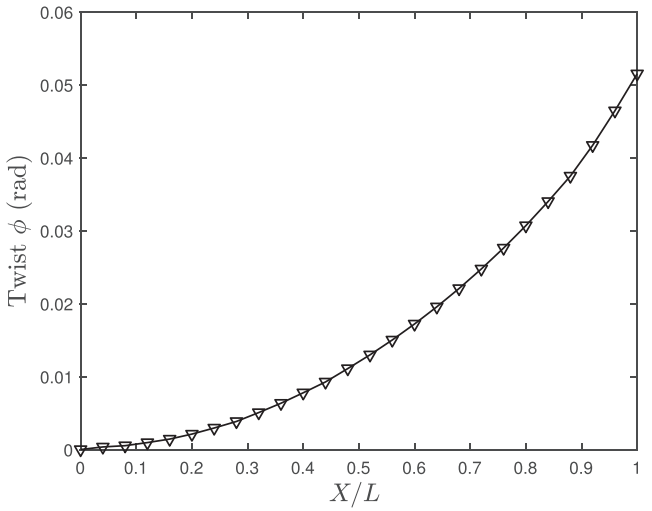

Fig. 20. The twist distribution of the spar for the Case 5 configuration ($\omega = 1000$ rpm, $m_p = 100$ g, $y_p = 80$ mm).

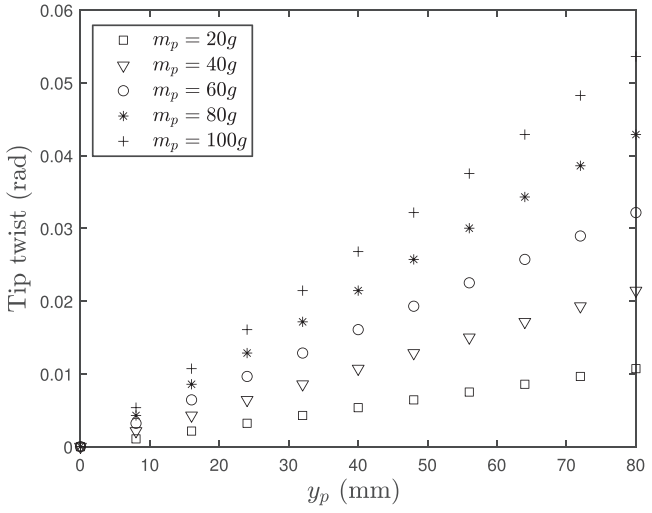

Fig. 21. Scaling relationship between the tip twist of the spar (Case 5) and the chordwise location of the mass for $\omega = 1000$ rpm.

6. Concluding remarks

A novel metamaterial was introduced to a composite blade which was able to produce a considerable twist in response to a lagwise bending moment, while the weight penalty was small. The bend-twist property is significantly dependent on the configuration of the unit cell. The metamaterial created with high aspect ratio resulted in a reduced bending moment to give a targeted twist, although the torsional stiffness was also reduced.

The maximum twist that can be achieved for each configuration was related to the failure mode: strength-controlled or buckling-controlled. In a strength-controlled failure, the increase in cell aspect ratio led to an increased twist limit. While for the buckling-controlled failure, the twist limit decreases dramatically with the aspect ratio due to the reduced buckling stress. Therefore the optimum cell configuration should be determined based on several key design considerations including the required torsional rigidity, targeted twist and prescribed bending moment that can be obtained from the actuator. The actuation mechanism for activating blade twist during rotation was examined, where a lagwise bending moment was generated by a movable mass at the tip. It was found that a significant twist was able to be induced by a reasonably small mass.

CRediT authorship contribution statement

Huaiyuan Gu: Conceptualization, Methodology, Formal analysis, Writing - original draft. **Alexander D. Shaw:** Supervision, Project administration, Writing - review & editing. **Mohammadreza Amoozgar:** Writing - review & editing. **Jiaying Zhang:** Writing - review & editing. **Chen Wang:** Writing - review & editing. **Michael I. Friswell:** Supervision, Project administration, Writing - review & editing.

Declaration of Competing Interest

The authors declare that they have no known competing financial interests or personal relationships that could have appeared to influence the work reported in this paper.

Acknowledgement

The authors acknowledge funding from the European Union's Horizon 2020 project 'Shape Adaptive Blades for Rotorcraft Efficiency (SABRE)', under grant agreement 723491.

References

[1] Li D, Zhao S, Ronch AD, Xiang J, Drofelnik J, Li Y, Zhang L, Wu Y, Kintscher M, Monner HP, Rudenko A, Guo S, Yin W, Kirn J, Storm S, Breuker RD. A review of modelling and analysis of morphing wings. Prog Aerosp Sci 2018;100:46–62.
[2] Barbarino S, Bilgen O, Ajaj RM, Friswell MI, Inman DJ. A review of morphing aircraft. J Intell Mater Syst Struct 2011;22:823–77.
[3] Motley MR, Barber RB. Study on composite bend-twist coupled wind turbine blade for passive load mitigation. Compos Struct 2019;213:173–89.
[4] Fincham JHS, Friswell MI. Aerodynamic optimisation of a camber morphing aerofoil. Aerosp Sci Technol 2015;27:245–55.
[5] Motley MR, Barber RB. Passive control of marine hydrokinetic turbine blades. Compos Struct 2014;110:245–55.
[6] Amoozgar MR, Shaw AD, Zhang J, Friswell MI. Composite blade twist modification by using a moving mass and stiffness tailoring. AIAA J 2019;57:4218–25.
[7] Sun J, Guan Q, Liu Y, Leng J. Morphing aircraft based on smart materials and structures: A state-of-the-art review. J Intell Mater Syst Struct 2016;27:2289–312.
[8] Ermakova A, Dayyani I. Shape morphing of aircraft wing: Status and challenges. Mater Des 2010;31:1284–92.
[9] Winkler M, Kress G. Influence of corrugation geometry on the substitute stiffness matrix of corrugated laminates. Compos Struct 2012;94:2827–33.
[10] Ermakova A, Dayyani I. Shape optimisation of composite corrugated morphing skins. Compos Part B 2017;115:87–101.
[11] Chen PC, Chopra I. Induced strain actuation of composite beams and rotor blades with embedded piezoceramic elements. Smart Mater Struct 1996;5:35–48.
[12] Chopra I. Review of state of art of smart structures and integrated systems. AIAA 2002;40:2145–87.
[13] Ameduri S, Concilio A. A shape memory alloy torsion actuator for static blade twist. J Intell Mater Syst Struct 2019;30:2605–26.
[14] HC H, CI. Aeroelastic stability of a composite blade, J Am Helicop Soc 1985;30:57–67..
[15] Chandra R, Stemple AD, Chopra I. Thin-walled composite beams under bending, torsional, and extensional loads. J Aircr 1990;27:619–26.
[16] Lobitz DW, Veers P. Aeroelastic behavior of twist-coupled hawt blades. ASME Wind Energy Symp 1998;21:17–24.
[17] Gibbs Y. Nasa armstrong fact sheet: X-29 advanced technology demonstrator aircraft. Nat Aeronaut Space Admin 2017.
[18] Li Y, Gu H, Pavier M, Coules H. Compressive behaviours of octet-truss lattices. Proc Inst Mech Eng Part C 2020.
[19] Gu H, Pavier M, Shterenlikht A. Experimental study of modulus, strength and toughness of 2d triangular lattices. Int J Solids Struct 2018;152–153:207–16.
[20] Gu H, Li S, Pavier M, Attallah MM, Paraskevoulakos C, Shterenlikht A. Fracture of three-dimensional lattices manufactured by selective laser melting. Int J Solids Struct 2019;180–181:147–59.
[21] Moongkhamklang P, Elzey DM, Wadley HN. Titanium matrix composite lattice structures. Compos Part A 2008;39:1264–72.
[22] Bettini P, Airoldi A, Sala G, Landro LD, Ruzzene M, Spadoni A. Composite chiral structures for morphing airfoils: Numerical analyses and development of a manufacturing process. Compos Part B 2010;41:133–47.
[23] Jamie M, Bruckner H, Jacques J, Chrystel R, Fabrizio S, Kevin P, Massimo R. The hexachiral prismatic wingbox concept. physica status solidi 2008;245:570–7.
[24] Hyeonu H, Jaehyung J, Doo-Man K, Chang-Soo J. Passive morphing airfoil with honeycombs. Proc ASME 2011 international mechanical engineering congress and exposition, vol. 1; 2011. p. 263–71..

[25] Zhong R, Fu M, Chen X, Zheng B, Hu L. A novel three-dimensional mechanical metamaterial with compression-torsion properties. Compos Struct 2019;226:111232.
[26] Wu W, Geng L, Niu Y, Qi D, Cui X, Fan D. Compression twist deformation of novel tetrachiral architected cylindrical tube inspired by towel gourd tendrils. Extr Mech Lett 2018;20:104–11.
[27] Nayakanti N, Tawfic S, Hart AJ. Twist-coupled kirigami cells and mechanisms. Extr Mech Lett 2018;21:17–24.
[28] Zheng B, Zhong R, Chen X, Fu M, Hu L. A novel metamaterial with tension-torsion coupling effect. Mater Des 2019;171:107700.
[29] Zhong R, Fu M, Yin Q, Xu O, Hu L. Special characteristics of tetrachiral honeycombs under large deformation. Int J Solids Struct 2019;169:116–76.
[30] Wu W, Hu W, Qian G, Liao H, Xu X, Berto F. Mechanical design and multifunctional applications of chiral mechanical metamaterials: A review. Mater Des 2019;180:107950.
[31] Wang DLMAJ. In-plane stiffness and yield strength of periodic metal honeycombs. J Eng Mater Technol 2004;126:137–56.
[32] ABAQUS/Standard User's Manual, Version 2017, Dassault Systèmes Simulia Corp, Providence, RI, United States; 2017..
[33] Aircraft Materials Al6082 data sheet [online] Available at: https://- www.aircraftmaterials.com/data/aluminium/6082.html [Accessed 12 July 2020]..
[34] BO 105 CB/CBS Approved rotorcraft flight manual, Eurocopter deutschland, a division of European Aeronautic Defence and Space Co. (EADS), Marseille Provence, France; 1993..
[35] Canale G, Rubino F, Weaver PM, Citarella R, Maligno A. Simplified and accurate stiffness of a prismatic anisotropic thin-walled box. Open Mech Eng J 2018;12:1–20.